RESEARCH ARTICLE

NANO · MICRO small
www.small-journal.com

Charge Distribution across Capped and Uncapped Infinite-Layer Neodymium Nickelate Thin Films

Aravind Raji, Guillaume Krieger, Nathalie Viart, Daniele Preziosi,* Jean-Pascal Rueff, and Alexandre Gloter**

Charge ordering (CO) phenomena have been widely debated in strongly-correlated electron systems mainly regarding their role in high-temperature superconductivity. Here, the structural and charge distribution in $NdNiO_2$ thin films prepared with and without capping layers, and characterized by the absence and presence of CO are elucidated. The microstructural and spectroscopic analysis is done by scanning transmission electron microscopy-electron energy loss spectroscopy (STEM-EELS) and hard X-ray photoemission spectroscopy (HAXPES). Capped samples show Ni^{1+}, with an out-of-plane (o-o-p) lattice parameter of around 3.30 Å indicating good stabilization of the infinite-layer structure. Bulk-sensitive HAXPES on Ni-2p shows weak satellite features indicating large charge-transfer energy. The uncapped samples evidence an increase of the o-o-p parameter up to 3.65 Å on the thin film top with a valence toward Ni^{2+} in this region. Here, 4D-STEM demonstrates (303)-oriented stripes which emerge from partially occupied apical oxygen. Those stripes form quasi-2D coherent domains viewed as rods in the reciprocal space with $\Delta q_z \approx 0.24$ reciprocal lattice units (r.l.u.) extension located at $Q = (\pm\frac{1}{3}, 0, \pm\frac{1}{3})$ and $(\pm\frac{2}{3}, 0, \pm\frac{2}{3})$ r.l.u. The stripes associated with oxygen re-intercalation concomitant with hole doping suggest a possible link to the previously reported CO in infinite-layer nickelate thin films.

1. Introduction

Discovery of superconductivity in Sr-doped infinite-layer nickelate thin films[1] has drawn an upsurge of interest being infinite-layer (IL) nickelates structurally and electronically analogous to cuprates. The particular way in which nickelates are prepared, that is presence/absence of a capping layer, combined with the subtle control of the crystal structure modification during the reduction process, is pivotal to attaining the zero-resistance state.[2–4] Apart from superconductivity, recent studies have also revealed the existence of charge ordering phenomena and magnetic excitations in IL-nickelate thin films,[5–8] the amplitudes of which mostly depend upon the particular sample preparation, that is presence/absence of a $SrTiO_3$ (STO) capping-layer and doping level. In particular, charge order (CO) has been observed in uncapped-IL $NdNiO_2$ samples and it is not much pronounced in the capped ones, which on the contrary host dispersing magnetic excitation with a bandwidth of circa 200 meV.[5,7] Such a marked dichotomy naturally raises the question of the structural stability of the uncapped IL-nickelate thin films, compared to that of the capped ones. Indeed, by considering previous reports about the perovskite nickelates,[9–11] one could infer on similar grounds, peculiar oxygen dynamics in IL-nickelates, such as vacancies or incomplete re-intercalation. The latter may distort the IL-crystalline structure, subsequently its electronic properties. Synthesis of IL-nickelates is obtained via a so-called topotactic reduction of the precursor perovskite $RNiO_3$ (RNO3, R being a rare-earth) thin films which involves removing apical oxygen in RNO3 thereby reducing it to the IL-nickelate $RNiO_2$ (IL-RNO2).[1] Such a pathway involves the reduction of the nominal valence of Ni from 3+ (in RNO3) to 1+ in (RNO2). This partially unstable state[12,13] can be prone to several structural and/or electronic reconstructions, and for a stable IL-RNO2 an $SrTiO_3$ (STO) capping layer has been used in the 2–25 nm thickness range.[4,14] On these grounds, the possible structural reconstructions in the uncapped IL-nickelate thin films stay unexplored. An atomically resolved structural and spectroscopic study which compares both capped and uncapped samples is necessary to obtain new insights to delineate a better understanding of such aforementioned contrasting differences.

A. Raji, A. Gloter
Laboratoire de Physique des Solides
CNRS
Université Paris-Saclay
Orsay 91405, France
E-mail: aravind.raji@universite-paris-saclay.fr;
alexandre.gloter@universite-paris-saclay.fr
A. Raji, J.-P. Rueff
Synchrotron SOLEIL, L'Orme des Merisiers
BP 48 St Aubin, Gif sur Yvette 91192, France
G. Krieger, N. Viart, D. Preziosi
Universite de Strasbourg
CNRS, IPCMS UMR 7504, Strasbourg F-67034, France
E-mail: daniele.preziosi@ipcms.unistra.fr
J.-P. Rueff
LCPMR
Sorbonne Université
CNRS, Paris 75005, France

The ORCID identification number(s) for the author(s) of this article can be found under https://doi.org/10.1002/smll.202304872

DOI: 10.1002/smll.202304872

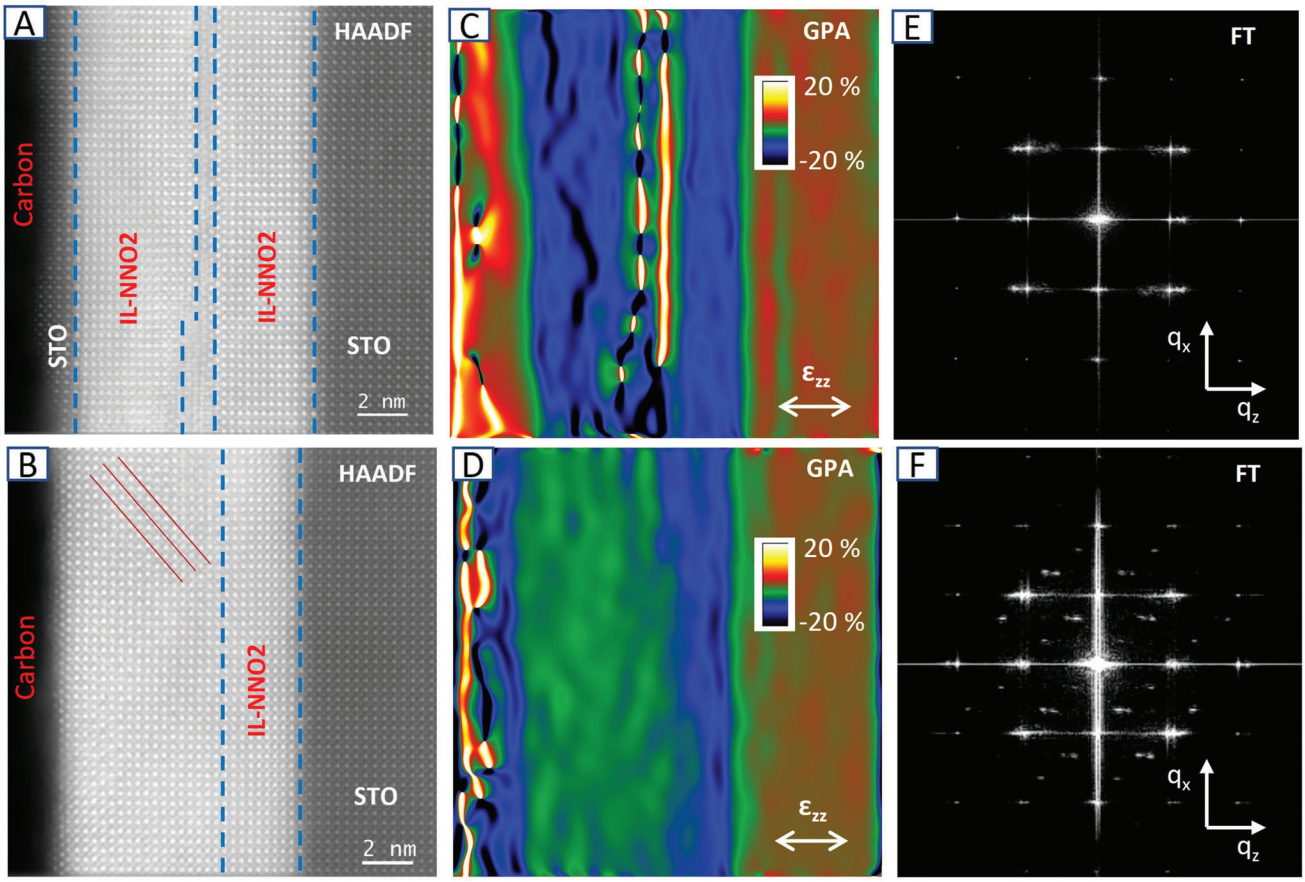

Figure 1. Comparison of capped (c-NNO2) and uncapped (uc-NNO2) infinite-layer nickelate thin films by HAADF, GPA, and FT. A,B) HAADF images showing the c-NNO2 (A) and uc-NNO2 (B), the faint contrast (303) stripe pattern as indicated by the red lines can be seen here. C,D) Maps of the o-o-p strain by GPA in c-NNO2 (C) and uc-NNO2 (D). Both capped and uncapped samples show a higher compression close to the film-substrate interface. c-NNO2 shows uniform compression of about 16% all over the sample, except for the small defect zone in the middle (C) and uc-NNO2 shows a less compressed zone toward the surface from the interface (D). E,F) Fourier transform of the HAADF image of the c-NNO2 (E) and uc-NNO2 (F).

Here we have investigated STO-capped and uncapped IL-$NdNiO_2$ thin films grown onto STO single crystals as substrate, hereafter referred to as c-NNO2 and uc-NNO2, respectively. By combining spectroscopic and microscopic techniques, specifically hard X-ray photoemission spectroscopy (HAXPES), scanning transmission electron microscopy (STEM) with monochromated electron energy loss spectroscopy (EELS), we conclude that the measured structural and electronic modifications are linked to a specific O re-intercalation path and charge reconstruction, which could contribute to the observed CO.

2. Results and Discussions

2.1. Real Space Structural Comparison

We start by discussing the real space structural aspects of both c-NNO2 and uc-NNO2 samples as obtained from STEM-HAADF imaging and geometrical phase analysis (GPA).[15] As shown in the STEM-HAADF images in **Figure 1**A,B, clear structural differences are observed between these two samples. The c-NNO2 shows an IL-structure in the majority of the thin-film, except the small off tilt-like defect in the middle as reported.[16] On the other hand, the uc-NNO2 shows an IL-structure near the interface with the STO substrate, with certain periodic faint contrast stripes on the top part of the thin-film which will be discussed in more details in the following section. Figure 1C shows the out-of-plane (o-o-p) strain maps (ϵ_{zz}) obtained by GPA in the c-NNO2, with reference to the STO o-o-p parameter of 3.91 Å. A compression of around 16% giving an o-o-p parameter of 3.30 Å is observed throughout the thin-film (blue region in Figure 1C), except in the defect region in the middle, indicating overall a good infinite-layer crystalline quality of this c-NNO2. Figure 1D shows such a strain map of the uc-NNO2, where a compression of around 16% is observed near the interface, giving an infinite-layer o-o-p parameter of 3.30 Å. However, the map shows a decrease of the compression to around 7% giving an o-o-p parameter of 3.65 Å on the top (green region in Figure 1D). The region of this o-o-p expansion coincides with the region where we observe certain low contrast stripes for this uc-NNO2 sample. The HAADF image in Figure 1B for the uc-NNO2 is from a region with more extended stripes, while other regions show stripes more restrained extending of only ≈2 nm from the surface (Figure S1, Supporting Information). The two samples show no differences in the in-plane strain (ϵ_{xx}) map (Figure S2, Supporting Information),

and a homogeneous in-plane parameter of 3.91 Å matching with STO is observed throughout the thin-film. The Fourier transform analysis shown in Figure 1E,F for the c-NNO2 and uc-NNO2, respectively further describes the differences observed in HAADF and GPA. The c-NNO2 shows a pair of spots along q_z around (101) reciprocal lattice units (r.l.u.) that matches with the different o-o-p parameters of STO and the infinite-layer structure. In contrast, the uc-NNO2 shows three spots along q_z around (101) r.l.u. indicating the o-o-p parameters of 3.91, 3.30, and 3.65 Å, respectively from the STO, infinite-layer, and the stripe region. Here, we also observe extended spots located at $q_x = q_z = \frac{1}{3}$ r.l.u., and $q_x = q_z = \frac{2}{3}$ r.l.u. The reciprocal lattice units , is defined with in-plane components $a = b = 3.91$ Å, and the out-of-plane lattice constant $c = 3.65$ Å. We chose the o-o-p as 3.65 Å because this is the parameter of the stripe region. Interestingly, similar faint contrast stripes can be observed in the STEM-HAADF image of other uncapped nickelate samples where CO is reported (Figure S5, Supporting Information, of ref. [6]), but were unnoticed. It further anticipates the connection between CO and these (303) stripes.

As mentioned by Krieger et al. in ref. [5], the CO signal decreases with the level of Sr-doping on $NdNiO_2$. In Figure S4, Supporting Information, we show our STEM-HAADF and GPA analysis on a 5% Sr-doped uncapped $Nd_{0.95}Sr_{0.05}NiO_2$ (uc-NSNO2) sample. We do not observe any stripes or o-o-p expansion as in the case of uc-NNO2. There are certain fluorite and Ruddlesden–Popper defects on the top of the sample, which are reportedly observed in these systems.[4] This also rises possible connection of CO to the presence of such charge-stripes as observed in uc-NNO2. Another aspect here is about the structural stability of undoped samples compared to the doped ones. As mentioned in ref. [6], a comparative study between uncapped samples that are both doped and undoped, indicates a difference in the o-o-p parameter for certain undoped samples. Also, as shown in the (Figures S3 and S4, Supporting Information), the Fourier transform shows no stripe intensities in the regions dominated by additional Fluorite-type defects, suggesting that defects can reduce re-intercalation processes. In the case of 5% Sr-doped sample, the presence of the dopant probably changes the chemical pathway for O re-intercalation. Doping possibly causes the stabilization of particular phases, that prevent the formation of the stripe order.

2.2. Reciprocal Space Analysis and 4D-STEM

Figure 2B shows a magnified Fourier transform analysis of the HAADF image showing stripes in the uc-NNO2 (Figure 2A). Here, the observed periodicity of the stripes contributes to extended rods in reciprocal space located at $q_x = q_z = \frac{1}{3}$ r.l.u., and $q_x = q_z = \frac{2}{3}$ r.l.u., with a $\Delta q_z \approx 0.24$ r.l.u. In the inverse-Fourier transform analysis Figure 2C, this appears as coherent domains that have a typical area of 10×1.5 nm^2. From our observations throughout the thin-film, these coherent domains appear as quasi-2D sheets of ≈1.5–2 nm extension along the o-o-p direction. When the stripes areas extend over a substantial part of the thin film, several sheets are coexisting within the depth as shown in Figure 2C, but areas with only one sheet can be also observed (Figure S1, Supporting Information). The stripe wavevector values reported here are in match with the CO wave-vector of $\mathbf{Q} = (\pm\frac{1}{3}, 0)$ r.l.u. as found in the previous studies of these samples,[5] and others[6,8] by studying the quasi-elastic scattering intensity of resonant inelastic X-ray scattering (RIXS) experiments. Recently, a q_z resolved resonant X-ray scattering study has been carried out on an infinite-layer $PrNiO_2$ thin film in which the CO has the $\mathbf{Q} = (\pm\frac{1}{3}, 0, 0.365)$ r.l.u. wavevector.[17] The reported value of $q_z = 0.365$ r.l.u. is within the extension of the rod in Figure 2B, extending between $q_z = 0.22$ to 0.46 r.l.u. In the Fourier transform in Figure 1E, no such rods are observed in the reciprocal space of the c-NNO2 sample. This goes in hand with the absence of CO reported in these c-NNO2 samples.[5] Figure 2D shows a magnified HAADF image in the stripe region, showing a faint dark contrast along the stripes, and between the rare-earth sites. A better understanding of this region is obtained from high-resolution 4D-STEM analysis. By collecting the whole diffraction pattern at each pixel, one can obtain a high resolution real space atomic mapping with good oxygen contrast.[18,19] Here, in Figure 2E, by employing such an integrated Centre of Mass (iCOM) analysis by 4D-STEM, we have a clear atomic-level mapping including oxygen. It indicates periodic partial intercalation of apical oxygen in the IL crystalline structure. If we consider a perovskite NNO3 structure, this could be interpreted as periodic apical oxygen vacancies (Vo). This finding is of paramount importance as it has been well demonstrated the influence of Vo in changing the local electronic structure especially in perovskite nickelates.[10] Since these Vo run along the stripes, they have the same periodicity as them, contributing to intensities at $\mathbf{Q} = (\pm\frac{1}{3}, 0, \pm\frac{1}{3})$ r.l.u. and $\mathbf{Q} = (\pm\frac{2}{3}, 0, \pm\frac{2}{3})$ r.l.u. in the reciprocal space.

The oxygen re-intercalations observed on the stripe-region of uc-NNO2, probably induce similar hole doping effects as in ref. [20] changing the Ni valence at these sites. The charge distribution is reflected in the spectroscopic studies, XAS showing a mixed valence and RIXS experiments already demonstrating a broken symmetry of the uc-NNO2[5] in reciprocal space. Since, now we have an understanding of the real space location of these stripes, HAXPES and monochromated STEM-EELS can probe the concomitant charge modulation as well.

2.3. HAXPES Analysis

HAXPES gives a depth resolved macroscopic understanding of the influence of this structural modification on the local electronic structure. **Figure 3**A,B shows the HAXPES data in both bulk-sensitive and surface-sensitive configurations. This is done to better discriminate signals stemming from the top and the bulk/interface regions of the samples. The bulk sensitive mode is obtained at 10° incidence angle of the incoming photons, with an estimated probing depth of 10 nm at 3000 eV as obtained by SESSA simulations.[21] In the surface sensitive mode, the incidence angle of 80° gives a probing depth of circa 2 nm at the same photon energy to get similar energy resolution. In both conditions, we compare the Ni 2p core level for the c-NNO2 and uc-NNO2. As expected, there are strong differences between the two samples and incidence conditions of the photons.

In the bulk-mode, it can be seen that the main Ni $2p_{3/2}$ peak shows a shift between capped and uncapped, with a shoulder at a high binding energy (HBE) and low binding energy (LBE), respectively. The separation between them is almost 1.6 eV. This difference gets stronger as we go to surface-sensitive

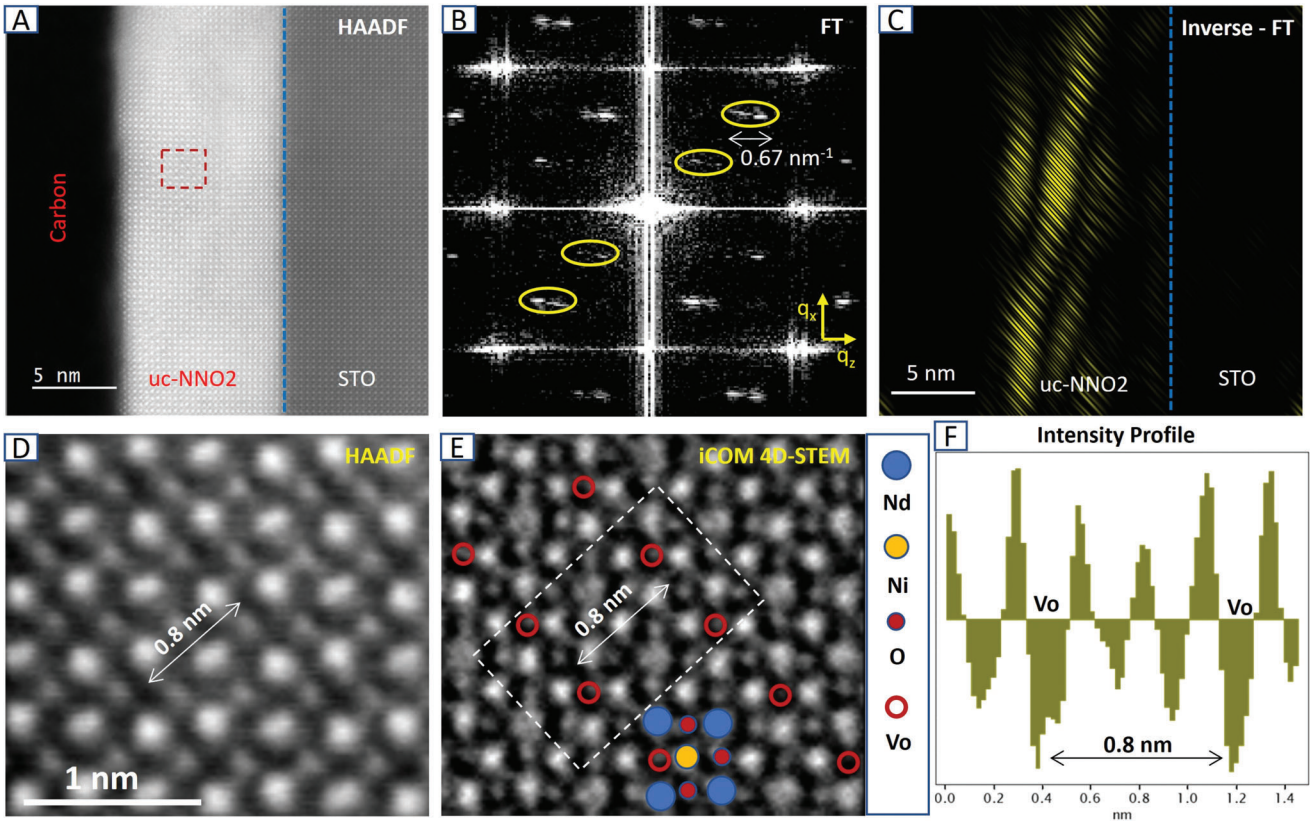

Figure 2. Combined reciprocal space and 4D-STEM analysis of the stripe region of the uc-NNO2. A) HAADF image showing the uc-NNO2 with stripes on the top part of the thin film. B) Magnified Fourier transform image showing an expanded unit cell and periodic rods located at $q_x = q_z = \frac{1}{3}$ r.l.u. and $q_x = q_z = \frac{2}{3}$ r.l.u., with a $\Delta q_z = 0.24$ r.l.u. C) The inverse-Fourier transform of the rods showing coherent domains that extends over 10 × 1.5 nm in size. D) A high magnification HAADF image from the stripe region (highlighted in A) showing periodic low contrast that gives rise to the stripes. E) 4D-STEM integrated Centre of Mass (iCOM) image in the same region showing partial apical oxygen intercalation, with absence of oxygen at the apical sites along the stripes. F) An intensity profile of the highlighted region of interest in the iCOM image that shows enhanced negative intensity further confirming oxygen vacancies along the stripes.

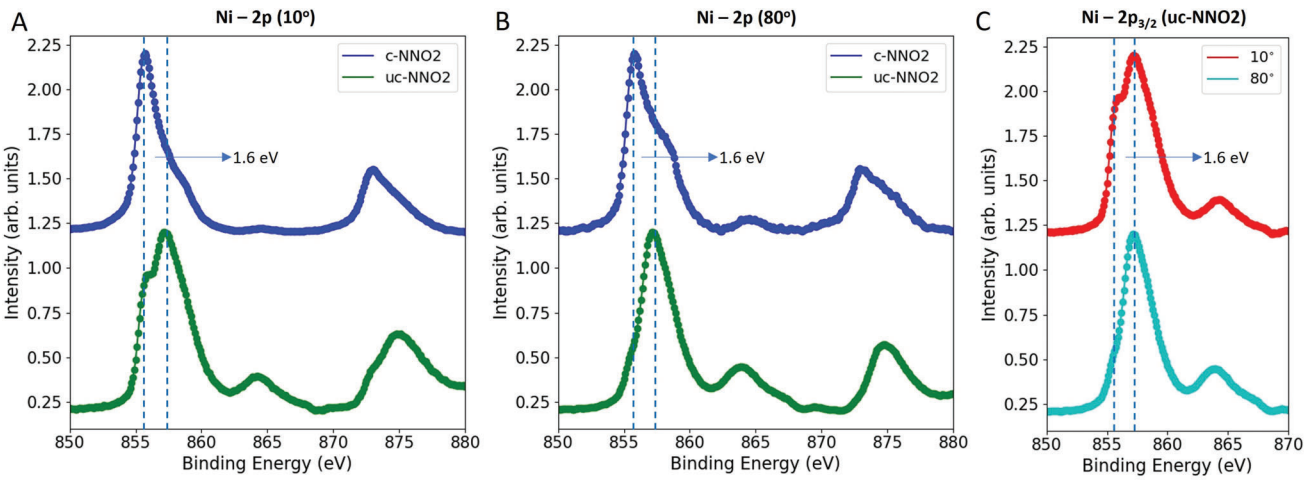

Figure 3. Hard X-ray photoemission (HAXPES) comparison of the Ni 2p core level of the c-NNO2 and uc-NNO2 samples. A,B) Comparison of Ni 2p photoemission in bulk sensitive 10° incidence condition (A) and surface sensitive 80° incidence condition from c-NNO2 and uc-NNO2 samples (B). C) A magnified comparison of Ni $2p_{3/2}$ photoemission at these two incidence conditions in the uc-NNO2 sample, clearly showing the potential decrease of the low binding energy shoulder in the 80° condition, indicating higher valence at the surface of uc-NNO2.

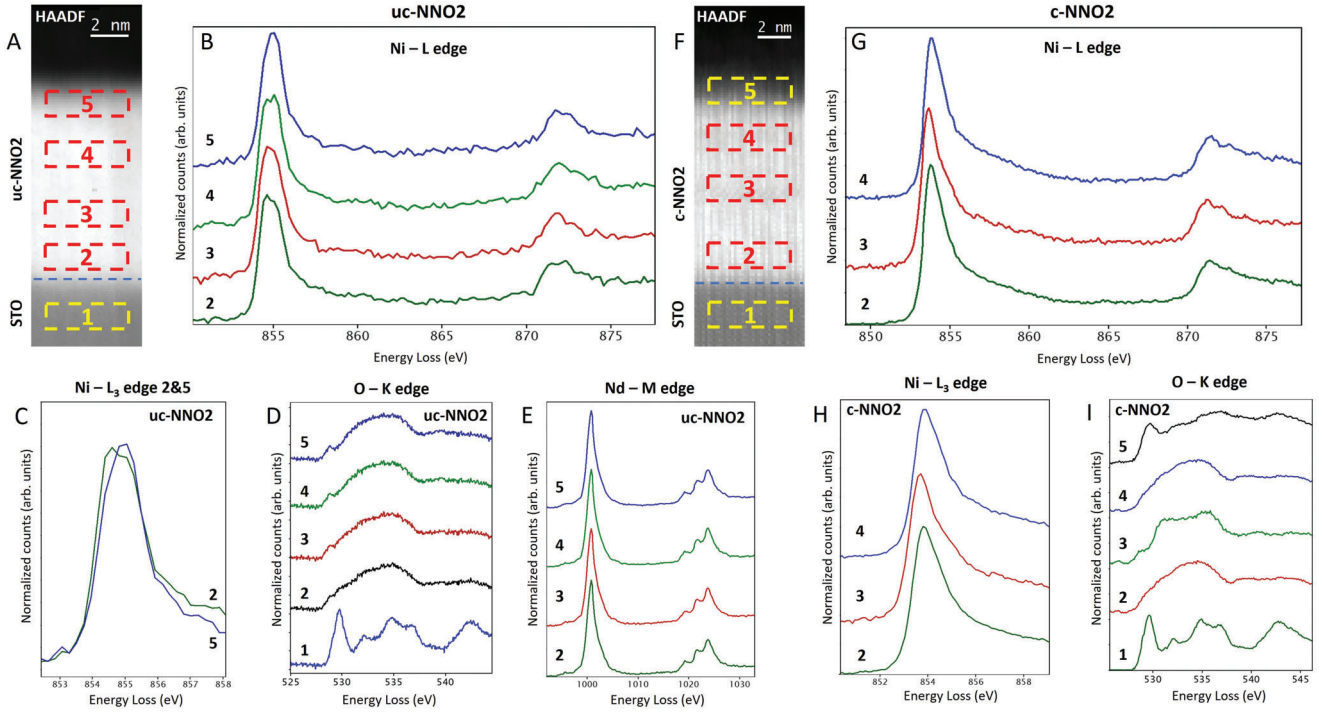

Figure 4. Monochromated electron energy loss spectroscopy (EELS) fine structure analysis of uc-NNO2 and c-NNO2 samples. A) HAADF image of the uc-NNO2 sample. B–F) EELS fine structure analysis of different regions labeled in the HAADF image of the uc-NNO2 sample. Ni-L edge comparison of the regions in the thin-film (B,C), (C) showing significant fine structure difference at the Ni-L_3 edge between the very interface region and the top of the thin-film. O-K edge fine structure showing emergence of a strong pre-peak around the top part of the thin-film (D). Nd-M edge fine structure showing no visible differences across the thin-film (E). HAADF image of the c-NNO2 sample (F). G–I) EELS fine structure analysis of different regions labeled in the HAADF image of the c-NNO2 sample. Ni-L edge comparison of the regions in the thin-film, showing no significant differences between them (G,H). O-K edge fine structure showing no differences at the two interfaces of the thin film, where absence of pre-peak in the fine structure indicates the existence of the perfect infinite-layer (I). A difference in fine structure is observed for the defect region in the middle and the spectrum looks similar as reported in ref. [14].

configuration, indicating a strong difference between the top part of the uc-NNO2 with that of the c-NNO2. The shift to high binding energy in the uc-NNO2 indicates a more oxidized Ni species, closer to Ni^{2+} than to Ni^{1+}, as in the case of IL-NNO2 structure. In Figure 3C, this difference is depicted more clearly by comparing the uc-NNO2 Ni-2p spectra at 10° and 80°. The decrease of LBE shoulder as we go more surface indicates the presence of more Ni^{2+} or higher valence at the top of the thin-film. Such a strong trend is not observed in the c-NNO2. A similar comparison of the Nd 3d photoemission spectra for both samples rendered no such peculiar differences of the core level (Figure S5, Supporting Information).

The c-NNO2 being a perfect infinite-layer thin film, hosts Ni^{1+} in a $3d^9$ configuration. It is to note that the c-NNO2 exhibit a very weak satellite peak located at almost 9 eV at higher binding energy from the main peak. It is rather different from previously reported soft X-ray PES that was having a strong satellite at only ≈6 eV from the main edge.[22] The discrepancy might occur, since our hard X-ray photoemission probes the bulk part of the capped sample, which is structurally a perfect infinite-layer. A weaker satellite peak at higher energy would indicate larger charge-transfer energy, pleading for a stronger Mott–Hubbard character[23] of the NNO2 than the one already inferred from the PES,[22] but more in accordance with the previously XAS and RIXS report of holed-doped system.[24]

In the case of uc-NNO2, as observed by 4D-STEM, there is still a partial presence of apical oxygen, resulting in hole doping that is changing the valence toward Ni^{2+}. The HAXPES of Figure 3 is characterized by a strong satellite peak located at a higher binding energy around 865 eV. The Ni species may be described as a mixture of Ni d^8 and Ni $d^9\underline{L}$ configuration, where $\underline{L}$ describes a hole in the ligand orbital, resulting in satellite and main edges. Comparing the Ni 2p photoemission spectrum from the top part of the uc-NNO2 with previously reported cases for NiO[25] and reduced $SrNiO_3$ nickelate,[26] the present case is more comparable to the latter. It indicates that the Ni ion here is not exactly as for Ni^{2+} in NiO which is characterized by a strong d^8[25] ground state, but bear more ligand-hole contribution. HAXPES is highly sensitive to changes in local chemistry, but it also gives an averaged macroscopic signal. The strong LBE shoulder that appears together with the main peak in the uc-NNO2 at 10° incidence (bulk-mode) is indeed due to this averaging of signals from Ni sites in the IL-NNO2 near the interface and the higher valence Ni at the surface as due to possible oxygen re-intercalation.

2.4. STEM-EELS Analysis

A higher spatial and energy resolved spectroscopic comparison between c-NNO2 and uc-NNO2 samples is obtained by

monochromated STEM-EELS. In **Figure 4**, such a spatial variation at Ni-L, O-K, and Nd-M edges is compared between both samples. In Figure 4B,C, a clear difference has been observed for the Ni-L_3 edge in the uc-NNO2, as we compare the spectrum from near the substrate interface, and to the top part of the thin film. The peak maxima show a shift to a higher energy loss at the top of the thin film. Figure 4D shows the O-K edge in this sample, where no pre-peak feature is observed near the interface as expected for an IL-NNO2, while having a stronger pre-peak feature around 527 eV going to the top of the thin film. In the case of the c-NNO2 sample, as shown in Figure 4G–I, we observe no differences for the Ni-L and O-K edges (except near the small defect area in the middle), confirming the existing data.[14] Interestingly, the O-K edge in the whole volume of the c-NNO2 sample shows no pre-peak feature except the central defective region, indicating the good stabilization of the IL crystalline structure.

The observed spatial spectroscopic differences in the uc-NNO2 are possibly caused by the local electronic reconstructions due to oxygen intercalation into the infinite-layer structure. The shift of Ni L_3 edge to a higher energy loss indicates a hole-doping effect toward a dominant Ni^{2+}.

The pre-peak in O-K edge at 527 eV stems from the hybridization between the O 2p and Ni 3d orbitals.[27] It is very strong in the case of perovskite $NdNiO_3$ with Ni being in a $3d^8\underline{L}$ ground state in the metallic phase. It almost disappears for an ideal infinite-layer $NdNiO_2$, where the Ni is in a $3d^9$ state, and also for NiO where the Ni is in a $3d^8$ state.[25] The observation of a small pre-peak in O-K at the top part of uc-NNO2, while corresponding primary to a Ni^{2+}, can be explained as these Ni^{2+} being a mixture of $3d^8$ and also some $3d^9\underline{L}$ electronic configuration, that is in accordance with the Ni 2p photoemission features in Figure 3. Similar to the Nd-3d photoemission spectra (Figure S5, Supporting Information), the Nd-M edge in Figure 4E shows no difference spatially in the uc-NNO2, and it can be attributed to the low sensitivity of rare earth elements to such local electronic/structural reconstructions.

3. Conclusion

Our multidimensional analysis demonstrates charge disproportionation associated with the formation of periodic stripes on the top region of an uc-NNO2 thin-film. The stripes are originating from partial oxygen re-intercalation into the IL-structure, hence, mimicking hole-doping effects. Spectroscopic signatures evidence the top part of the uc-NNO2 is mixed valence composed of Ni^{1+} (d^9) and Ni^{2+} (d^8 with possibly some $d^9\underline{L}$ configuration due to a larger degree of hybridization). Since a possible origin of this additional charge on Ni may be attributed to oxygen re-intercalation (hole-doping), this charge distribution is influenced by the (303) periodicity of the stripes. The stripes form quasi-2D coherent domains of diverse spatial extensions throughout the thin-film. They give extended rods in reciprocal space at $\mathbf{Q} = (\pm\frac{1}{3}, 0, \pm\frac{1}{3})$ r.l.u. and $\mathbf{Q} = (\pm\frac{2}{3}, 0, \pm\frac{2}{3})$ r.l.u., with the former value fully comparable with the CO wavevector $\mathbf{Q} = (\frac{1}{3}, 0)$ r.l.u. observed in this sample. No such chemical and structural modification is observed in c-NNO2 and 5% Sr-doped uc-NSNO2, the latter closely connected with the observation of diminished CO. In the case of the uc-NNO2 studied here, the intercalation of oxygen to the apical sites essentially changes the local structure of these regions of the thin-film. Understanding the spatial configuration of oxygen intercalation, its energetic favorability and dynamics is another aspect along this direction.

4. Experimental Section

Sample Preparation: Perovskite precursor thin films had been grown by pulsed laser deposition technique assisted by reflection high energy electron diffraction onto STO substrates (CODEX) that underwent the standard HF-etching and annealing processes to obtain single terminated TiO_2-terrace morphology. The STO capping layer of three unit cells, when present, had been grown just after the perovskite nickelate and prior to the topotactic reduction as already mentioned elsewhere.[28]

High Resolution STEM-EELS and 4D-STEM: Cross sectional transition electron microscopy (TEM) lamellae were prepared using a focused ion beam (FIB) technique (D. Troadec at IEMN facility Lille, France and at C2N, University of Paris-Saclay, France). Before FIB lamellae preparation, around 20 nm of amorphous carbon was deposited on top for protection. The HAADF imaging and 4D-STEM was carried out in a NION UltraSTEM 200 C3/C5-corrected scanning transmission electron microscope (STEM). The experiments were done at 100 keV with a probe current of ≈10 pA and convergence semi-angles of 30 mrad. A MerlinEM (Quantum Detectors Ltd) in a 4 × 1 configuration (1024 × 256) had been installed on a Gatan ENFINA spectrometer mounted on the microscope.[29] The EELS spectra were obtained using the full 4 × 1 configuration and the 4D-STEM by selecting only one of the chips (256 × 256 pixels). For 4D-STEM, the EELS spectrometer was set into non-energy dispersive trajectories and 6-bit detector mode that gave a diffraction pattern with a good signal to noise ratio without compromising much on the scanning speed was used. The geometrical phase analysis (GPA)[15] had been done choosing the STO substrate with 3.91 Å as a reference parameter. The lattice parameters of the IL-NNO2 for capped and un-capped were estimated by averaging the GPA maps over typical rectangular areas of ≈20 (in-plane) × 2 (out-of-plane) nm giving a strain accuracy determination better than 1%, id est, better than 0.04 Å for the lattice parameters.

The monochromated EELS had been done using a NION CHROMATEM STEM at 100 keV with a probe current of ≈30 pA, a convergence semi-angles of 25 mrad and an energy resolution around 70 meV. The EELS detection was also done with a MerlinEM in a 4 × 1 configuration (1024 × 256) that had been installed on a Nion IRIS spectrometer mounted on the microscope.

HAXPES Measurements: The measurements were carried out at the GALAXIES beamline at the SOLEIL synchrotron[30] on the HAXPES endstation[31] using a photon energy of 3000 eV, with an incidence angle of 10° for the bulk sensitive measurements and 80° for the surface sensitive measurements. The bulk sensitivity is defined from the SESSA simulations[21] that give a probing depth of around 10 nm for 10° incidence and around 2 nm for 80° incidence. About 95% of the detected signal would be from the elements within these estimated probing depths. The synchrotron operated with a ring current of 450 mA, giving an intensity of 3.4×10^{13} photons s^{-1} at 3000 eV, which was then reduced using a built-in filter to 5% of the original intensity. The photoelectrons were detected using a SCIENTA Omicron EW4000 HAXPES hemispherical analyzer and a Shirley background[32] was removed prior to fitting the core levels spectra.

Supporting Information

Supporting Information is available from the Wiley Online Library or from the author.

Acknowledgements

This work was supported by the French National Research Agency (ANR) through the ANR-21-CE08-0021-01 "ANR FOXIES" and within the

Interdisciplinary Thematic Institute QMat, as part of the ITI 2021 2028 program of the University of Strasbourg, CNRS and Inserm. It was supported by IdEx Unistra (ANR 10 IDEX 0002) and by SFRI STRAT'US project (ANR 20 SFRI 0012) and ANR-11-LABX-0058-NIE and ANR-17-EURE-0024 under the framework of the French Investments for the Future Program. A.R. acknowledges financing from LABEX NanoSaclay and H2020 for the doctoral funding. Nion CHROMATEM at LPS Orsay and the FIB at C2N, University of Paris-Saclay were accessed in the TEMPOS project framework (ANR 10-EQPX-0050). The authors acknowledge SOLEIL Synchrotron for provision of beamtime under proposals 20211467 and 20221574. The authors thank M. Salluzzo and G. Ghiringhelli for critical reading of the manuscript.

Conflict of Interest

The authors declare no conflict of interest.

Data Availability Statement

The data that support the findings of this study are available from the corresponding author upon reasonable request.

Keywords

charge order, hard X-ray photoemission spectroscopy, infinite-layer nickelates, STEM-EELS

Received: June 9, 2023
Revised: July 7, 2023
Published online:

[1] D. Li, K. Lee, B. Y. Wang, M. Osada, S. Crossley, H. R. Lee, Y. Cui, Y. Hikita, H. Y. Hwang, *Nature* **2019**, *572*, 624.
[2] X. Yang, M. Li, Z. Ding, L. Li, C. Ji, G. Wu, *Adv. Quantum Technol.* **2023**, *6*, 2200065.
[3] L. E. Chow, A. Ariando, *Front. Phys.* **2022**, *10*, 834658.
[4] K. Lee, B. H. Goodge, D. Li, M. Osada, B. Y. Wang, Y. Cui, L. F. Kourkoutis, H. Y. Hwang, *APL Mater.* **2020**, *8*, 041107.
[5] G. Krieger, L. Martinelli, S. Zeng, L. Chow, K. Kummer, R. Arpaia, M. M. Sala, N. B. Brookes, A. Ariando, N. Viart, M. Salluzzo, G. Ghiringhelli, D. Preziosi, *Phys. Rev. Lett.* **2022**, *129*, 027002.
[6] C. C. Tam, J. Choi, X. Ding, S. Agrestini, A. Nag, M. Wu, B. Huang, H. Luo, P. Gao, M. García-Fernández, L. Qiao, K.-J. Zhou, *Nat. Mater.* **2022**, *21*, 1116.
[7] H. Lu, M. Rossi, A. Nag, M. Osada, D. Li, K. Lee, B. Wang, M. Garcia-Fernandez, S. Agrestini, Z. Shen, E. M. Been, B. Moritz, T. P. Devereaux, J. Zaanen, H. Y. Hwang, K.-J. Zhou, W. S. Lee, *Science* **2021**, *373*, 213.
[8] M. Rossi, M. Osada, J. Choi, S. Agrestini, D. Jost, Y. Lee, H. Lu, B. Y. Wang, K. Lee, A. Nag, Y.-D. Chuang, C.-T. Kuo, S.-J. Lee, B. Moritz, T. P. Devereaux, Z.-X. Shen, J.-S. Lee, K.-J. Zhou, H. Y. Hwang, W.-S. Lee, *Nat. Phys.* **2022**, *18*, 869.
[9] L. Wang, S. Dash, L. Chang, L. You, Y. Feng, X. He, K.-j. Jin, Y. Zhou, H. G. Ong, P. Ren, S. Wang, L. Chen, J. Wang, *ACS Appl. Mater. Interfaces* **2016**, *8*, 9769.
[10] M. Kotiuga, Z. Zhang, J. Li, F. Rodolakis, H. Zhou, R. Sutarto, F. He, Q. Wang, Y. Sun, Y. Wang, N. A. Aghamiri, S. B. Hancock, L. P. Rokhinson, D. P. Landau, Y. Abate, J. W. Freeland, R. Comin, S. Ramanathan, K. M. Rabe, *Proc. Natl. Acad. Sci. USA* **2019**, *116*, 21992.
[11] Y. Shin, J. M. Rondinelli, *Phys. Rev. Res.* **2022**, *4*, L022069.
[12] M. Hayward, M. Green, M. Rosseinsky, J. Sloan, *J. Am. Chem. Soc.* **1999**, *121*, 8843.
[13] A. Subedi, *Phys. Rev. Mater.* **2023**, *7*, 024801.
[14] B. H. Goodge, D. Li, K. Lee, M. Osada, B. Y. Wang, G. A. Sawatzky, H. Y. Hwang, L. F. Kourkoutis, *Proc. Natl. Acad. Sci. USA* **2021**, *118*, e2007683118.
[15] M. Hÿtch, E. Snoeck, R. Kilaas, *Ultramicroscopy* **1998**, *74*, 131.
[16] S. Zeng, C. S. Tang, X. Yin, C. Li, M. Li, Z. Huang, J. Hu, W. Liu, G. J. Omar, H. Jani, Z. S. Lim, K. Han, D. Wan, P. Yang, S. J. Pennycook, A. T. S. Wee, A. Ariando, *Phys. Rev. Lett.* **2020**, *125*, 147003.
[17] X. Ren, R. Sutarto, Q. Gao, Q. Wang, J. Li, Y. Wang, T. Xiang, J. Hu, F.-C. Zhang, J. Chang, R. Comin, X. J. Zhou, Z. Zhu, *arXiv:2303.02865*, **2023**.
[18] Q. Jia, A. Gloter, *Adv. Mater. Interfaces* **2023**, *10*, 2202165.
[19] C. Yang, Y. Wang, W. Sigle, P. A. van Aken, *Nano Lett.* **2021**, *21*, 9138.
[20] H. Zhao, Z. Ren, B. Rachmilowitz, J. Schneeloch, R. Zhong, G. Gu, Z. Wang, I. Zeljkovic, *Nat. Mater.* **2019**, *18*, 103.
[21] W. Smekal, W. S. Werner, C. J. Powell, *Surf. Interface Anal.* **2005**, *37*, 1059.
[22] K. Higashi, M. Winder, J. Kuneš, A. Hariki, *Phys. Rev. X* **2021**, *11*, 041009.
[23] J. Zaanen, G. Sawatzky, J. Allen, *Phys. Rev. Lett.* **1985**, *55*, 418.
[24] M. Rossi, H. Lu, A. Nag, D. Li, M. Osada, K. Lee, B. Y. Wang, S. Agrestini, M. Garcia-Fernandez, J. Kas, Y.-D. Chuang, Z. X. Shen, H. Y. Hwang, B. Moritz, K.-J. Zhou, T. P. Devereaux, W. S. Lee, *Phys. Rev. B* **2021**, *104*, L220505.
[25] G. Van der Laan, J. Zaanen, G. Sawatzky, R. Karnatak, J.-M. Esteva, *Phys. Rev. B* **1986**, *33*, 4253.
[26] L. Wang, Z. Yang, X. Yin, S. D. Taylor, X. He, C. S. Tang, M. E. Bowden, J. Zhao, J. Wang, J. Liu, D. E. Perea, L. Wangoh, A. T. S. Wee, H. Zhou, S. A. Chambers, Y. Du, *Sci. Adv.* **2021**, *7*, eabe2866.
[27] F. De Groot, M. Grioni, J. C. Fuggle, J. Ghijsen, G. A. Sawatzky, H. Petersen, *Phys. Rev. B* **1989**, *40*, 5715.
[28] G. Krieger, A. Raji, L. Schlur, G. Versini, C. Bouillet, M. Lenertz, J. Robert, A. Gloter, N. Viart, D. Preziosi, *J. Phys. D: Appl. Phys.* **2022**, *56*, 024003.
[29] M. Tencé, J.-D. Blazit, X. Li, M. Krajnak, E. N. del Busto, R. Skogeby, L. Cambou, M. Kociak, O. Stephan, A. Gloter, *Microsc. Microanal.* **2020**, *26*, 1940.
[30] J.-P. Rueff, J. M. Ablett, D. Céolin, D. Prieur, T. Moreno, V. Balédent, B. Lassalle, J. E. Rault, M. Simon, A. Shukla, *J. Synchrotron Radiat.* **2015**, *22*, 175.
[31] D. Céolin, J. Ablett, D. Prieur, T. Moreno, J.-P. Rueff, T. Marchenko, L. Journel, R. Guillemin, B. Pilette, T. Marin, M. Simon, *J. Electron Spectrosc. Relat. Phenom.* **2013**, *190*, 188.
[32] D. A. Shirley, *Phys. Rev. B* **1972**, *5*, 4709.